3D Single-Molecule Imaging of Transmembrane Signaling by Targeting Nanodiamonds

*Wenliang Liu, Fenglei Yu, Jianbo Yang, Bo Xiang, Peng Xiao, and Li Wang**

Fluorescent nanodiamonds (FNDs) have recently emerged as promising probes for imaging applications. A significant limitation of the applications is the use of FNDs as endogenous protein tags for long-term 3D single molecule imaging to gain critical understanding of the underlying mechanism such as transmembrane signaling. Here, FNDs conjugated with transforming growth factor (TGF) are developed as an imaging probe for endogenous TGF-beta (TGF-β) receptor labeling and 3D single molecule imaging. FNDs display higher localization accuracy in 3D than organic dye making it an ideal candidate for nanoscopy applications. The real-time dynamics of TGF-β receptors after binding conjugated FNDs and in cells treated with therapeutic small molecule kinase inhibitors (SMI) are further monitored. The Bayesian treatment of hidden Markov models confirms and quantifies three different diffusive states and the transition rates between the three states. The kinetic reaction favors a faster diffusion population after therapeutic SMI treatment. The results show that immobilized TGF-β is critical for active signaling. SMI treatment can release TGF-β from the signaling complex. The results demonstrate the reported method that provides a powerful technique to study the mechanism of transmembrane signaling and valuable insights for developing better therapeutic for TGF-β-associated cancers.

1. Introduction

The transforming growth factor-beta (TGF-β) signaling pathway is important during cell development and is tightly regulated to ensure its proper physiological functions.[1,2] TGF-β acts as a tumor suppressor in normal epithelial cells and in early stages of tumors but can activate the growth and invasion of cancer cells in advanced stages.[3] Thus, this pathway is an attractive target for cancer therapeutics that simultaneously target the tumor and its microenvironment.[4] Although it is known that interactions between TGF-β and its ligand can lead to immune suppression and the metastasis of cancer cells, the exact mechanisms underlying this are unknown.

TGF-β ligands initiate signaling by binding to a type II receptor serine/threonine kinase and subsequently recruiting a type I receptor. The type II receptor phosphorylates the receptor I kinase domain.[5] This binding complex propagates the signal by phosphorylating SMAD proteins and other cofactors. Finally, SMAD proteins that have been translocated into the nucleus regulate the transcription of the target gene.[6] Despite much progress over the past decade, critical understanding of the dynamics and function of TGF-β transmembrane signaling with high temporal and spatial resolution is hampered by technical limitations. An integrated understanding of TGF-β is critical for the development of cancer targeting therapies.[7]

Traditional bioimaging and biochemical techniques provide limited information regarding detecting ligand–receptor interactions and subsequent downstream signaling. Fluorescent organic dyes and genetically coded protein tags that are used for such assays are relatively dim and photobleach after a short amount of time. These drawbacks prevent observation of the dynamic behaviors of biomolecules over a prolonged time period. Fluorescent nanodiamonds (FNDs) containing negatively charged nitrogen-vacancy (NV^-) centers are fluorescent sources with unique optical properties, including broad excitation and emission spectra and superior brightness without photobleaching.[8] Compared to quantum dots (QDs), FNDs do not photoblink and are nontoxic to cells,[9] which makes them ideal for biomedical applications. FNDs have been used as optical labels for regular epifluorescence imaging in live mammalian cells,[10–12] as magnetic resonance imaging imaging agents,[13] as drug delivery systems,[14,15] and to track the

Dr. W. Liu, Prof. F. Yu, Dr. L. Wang
Department of Thoracic Surgery
The Second Xiangya Hospital
of Central South University
139 Renmin Middle Road
Changsha, Hunan 410011, P. R. China
E-mail: li-wang@csu.edu.cn
Dr. J. Yang
Department of Laboratory
Medicine and Pathology
Masonic Cancer Center
University of Minnesota
MMC 609, 420 Delaware St SE
Minneapolis, MN 55455, USA
Dr. B. Xiang, Dr. L. Wang
Group of NanoMaterials
Cancer Research Institute
Central South University
110 Xiangya Road
Changsha, Hunan 410078, P. R. China
P. Xiao
Departments of Thoracic Surgery
The Third Xiangya Hospital
of Central South University
138 Tongzi Po Road
Changsha, Hunan 410013, P. R. China

DOI: 10.1002/adfm.201502883

movement of a single particle in the cytoplasm.[16] While FNDs have many benefits in in vivo bioimaging, FNDs have not been used as an endogenous protein tag in long-term 3D single molecule imaging. Developing this technology would allow the investigation of the dynamic behavior of biomolecules, such as transmembrane signaling.

In the present work, we demonstrate the use of FNDs as a general fluorescent tag for specific endogenous protein labeling and 3D single molecule imaging in live cells. Due to its superior optical properties, we could achieve approximately average of 8 nm in *xy* and 16 nm in *z* localization accuracy in 3D localization microscopy in the focal plane in cells, providing much higher localization precision than organic dye. By combining 3D astigmatism single molecule imaging analysis with FNDs, we observed and quantified 3D real-time dynamics of TGF-β receptors. Single molecule analysis determined three distinct diffusive states and the kinetic rates between those states in untreated and small molecule kinase inhibitor (SMI)-treated cells. We found that the kinetic reaction favors intermediate and fast diffusion populations after SMI treatment. Our experiments provide a general platform to study transmembrane signaling function and dynamics. Future application of this method will allow the development of TGF-targeted therapeutics based on signaling dynamics.

2. Results and Discussion

2.1. Optical Properties of Bioconjugated FND for Nanoscopy

We first conjugated NH_2-PEG-COOH to FNDs through the interaction between the amino group of polyethylene glycol (PEG) and the carboxyl group on the surface of FNDs as previously reported.[17] The carboxyl group of PEG was then bound by streptavidin (SA). Aggregation is a major concern for nanoparticles under physiological conditions, such as cell culture medium. To minimize aggregation, we used bovine serum albumin (BSA) to coat the FND surface through simple physical adsorption to decrease nonspecific interactions (FND-TGF-BSA). The biotin-TGF was attached to the FNDs through SA–biotin interactions (**Figure 1**a). In order to estimate the number of TGFs attached to a single FND, the concentration of FND was first determined through fluorescence correlation spectroscopy (FCS) (Equations (1), (2), (11), and (12)). Next, the protein concentration is determined using absorbance at 280 nm. The number of TGFs attached to a single FND was calculated as 1.2, which suggests that the as-prepared FND-TGF is suitable for single molecule imaging.

To characterize the dispersibility and photophysics of FND-TGF-BSA, we placed FNDs on the surface of cleaned coverslips. Individual spots can be clearly visualized through total internal reflection fluorescence microscope (TIRF) illumination (Figure 1b). Little aggregation was observed with TIRF imaging, demonstrating that the FND-TGF-BSA has good dispersity. We monitored the fluorescence intensity of FNDs for 5 min using a 561 nm continous wave (CW) laser (≈2 KW cm^{-2}). The single molecule fluorescence trace showed that FNDs do not photobleach or photoblink, suggesting that they are ideal for single molecule imaging (Figure 1c).

In order to further quantify the size and dispersibility of FND-TGF-BSA in a physiologically relevant condition, we applied FCS to monitor the FNDs in a high-salt solution (0.15 M KCl), which mimics intracellular environments.[18] FCS monitors the fluorescence molecules diffusing in and out in a tightly focused confocal volume. Thus it gives rise to fluorescence fluctuation intensity as a function of time and measures the diffusion and concentration parameters.[19] The autocorrelation function of the FND-TGF-BSA (Figure 1d) fit well with a single component 3D diffusion model. The diffusion coefficient (D) of the FNDs was calculated as 10.6 $\mu m^2\ s^{-1}$ (Equations (1)–(5)). The counts per second per molecule (cpsm) of FND-TGF-BSA was calculated through multiplying the G(0) (Equation (10)) by average count rate. As calculated, FND-TGF-BSA showed 43 000 cpsm. The size of the FND-TGF-BSA was then estimated by the Einstein–Stokes relationship $D = kT/(6\pi\eta\gamma)$, where k is the Boltzmann constant, T is the temperature, η is the viscosity of liquid, and γ is the radius. The average hydrodynamic diameter of diffusing FND-TGF-BSA was estimated to be 46 nm based on the FCS measurements. The autocorrelation curve of FND-TGF-BSA showed that a single component is sufficient to describe diffusion behavior, again suggesting the FNDs have

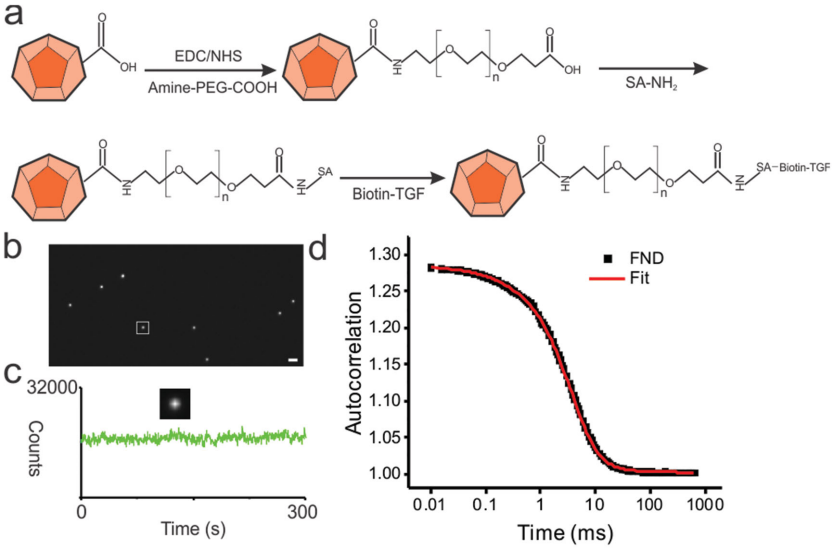

Figure 1. Bioconjugation of nanodiamonds and their superior optical properties. a) The acid-wash nanodiamond surface was activated with EDAC and NHS to form amine-reactive termini. The nanodiamond was then conjugated with carboxyl PEG amines. SA was grafted onto the nanodiamond through amide bond formation. Then, the SA-conjugated nanodiamond was connected to TGF-biotin through the SA–biotin interaction. b) In vitro single molecule imaging of FNDs acquired by total internal reflection fluorescence (TIRF) microscopy. Scale bar: 1 μm. c) Fluorescence intensity of a single FND-TGF-BSA as a function of time. Inset: Fluorescence image of a single FND corresponding to the white square region shown in (b). d) FCS measurement of FND-TGF-BSA. The autocorrelation function was fitted with a 3D free diffusion model. The fitted diffusion time was 1.85 ms corresponding to diffusion coefficient of 10.6 $\mu m^2\ s^{-1}$.

good dispersity with no obvious aggregation. Dynamic light scattering (DLS) was performed to further study the size distribution. The majority (96.3%) of the FND-TGF showed a narrow peak with diameter of ≈48 nm demonstrating FND-TGF had good dispersity with narrow size distribution (Figure S1, Supporting Information). This result is in good agreement with our FCS measurement. Furthermore, we applied transmission electron microscopy (TEM) to detect morphology and size of FND-TGF-BSA. The as-prepared FND-TGF-BSA showed a nice morphology and uniform distribution and little aggregation was detected (Figure S2a,b, Supporting Information).

Next, we investigated the 3D imaging capability of FNDs by localization microscopy. In a normal 2D microscopy setup, the point-spread function (PSF) is symmetrical and therefore it is not possible to determine the z position, which is located either below or above the focus. We used a cylinder lens to induce the astigmatism of PSF and therefore the precise z position of a single molecule can be localized as described previously.[20,21] In our system, an oil-immersion objective (Nikon Apo TIRF 100X, 1.49 NA) was used. The cylinder lens (f = 1 m) was inserted into the emission pathway between the tube lens and electron-multiplying charge-coupled device (EMCCD) (**Figure 2**a). To generate a calibration curve of W_x and W_y as a function of z, a single FND on a clean coverslip at different z positions was imaged using a piezo stage with a step size of 10 nm. A different z position of the FND displayed varied orientation and ellipticity (Figure 2b). The center of the individual spot provided the x–y localization and the ellipticity provided the z localization (Equations (6) and (7)). The detected spots that appeared too wide and too elliptical were rejected for calibration (Fitting radius ≥ 6 pixel). We then determined the calibration curve by quantifying 25 different FNDs on the coverslip. We found the sensitive z range of FNDs to be between −360 and 360 nm (Figure 2c). The localization accuracy is significant for single molecule microscopy applications and analysis. To quantify localization accuracy, single FNDs were imaged continuously for 1000 frames. The in vitro single molecule experiment was performed with the same excitation power and acquisition conditions (integration time and electron-multiplying (EM) gain) to generate similar counts (signal) which is comparable to the case in live cells. Each frame was then fitted with a 2D asymmetric Gaussian function. The distribution of the x, y, and z localizations were fitted with a Gaussian function (σ = 6 nm for xy, σ = 15 nm for z) (Figure S3a,b, Supporting Information). In order to better characterize the localization accuracy of FND in cells, we first incubated FND-TGF-BSA with HCC827 cells and the cells were fixed subsequently. Since the intrinsic fluorescence signal of FND varies with the number of NV centers available in a particle, the localization accuracy would vary with different signal to background ratio (SBR) which is defined as dividing the signal by background. The SBR for FND-BSA-TGF population in the fixed cells (n = 322) was first quantified. The distribution of SBR showed a broad range due to the varied NV centers per particle (Figure 2d). The 95% confidence interval of SBR was estimated from 5 to 17 based on the 5% and 95% quantile for nonnormal distribution data (Figure 2d). We therefore determined the localization accuracy under different SBR: 15 nm in xy and 30 nm in z for SBR = 5 and 6 nm in xy and 15 nm in z for SBR = 17 (Figure 2e). The mean of SBR was found to be 12 which corresponding to the localization accuracy of FND in fixed cell about 8 nm in xy and 16 nm in z. The average localization error of FND in fixed cells slightly increase

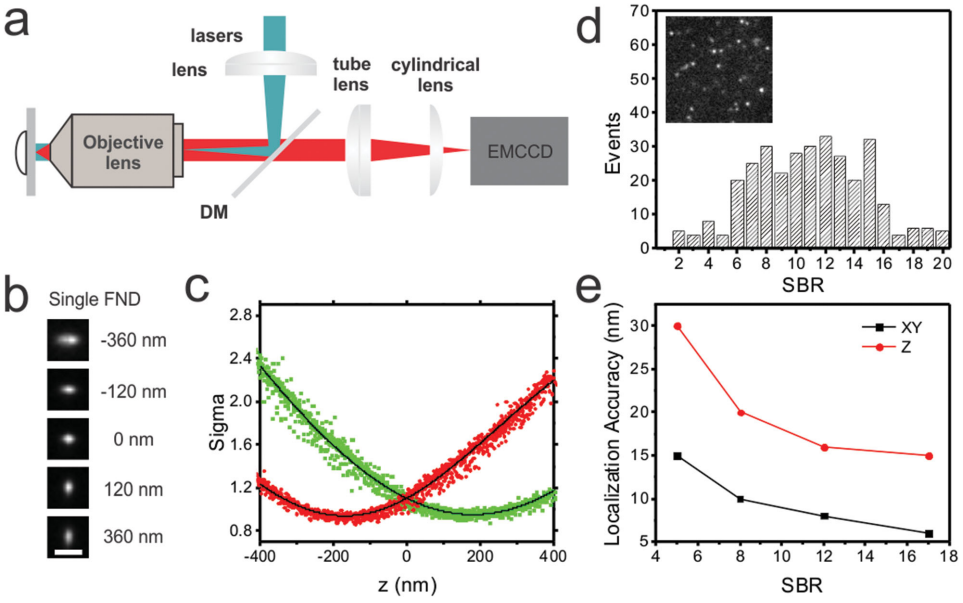

Figure 2. 3D imaging of a single FND. a) Optical layout of wide-field microscopy for 3D FND single molecule tracking. Lasers (561 nm) were reflected by a dichroic mirror to excite the FND. The emission was collected by the same objective lens. A cylindrical lens (f = 1 m) was placed in front of the EMCCD to induce astigmatism. b) Single molecule imaging of FND at different z positions. Notice that different z positions display varied orientations and ellipticities. Scale bar: 1 μm. c) Calibration curve of PSF widths W_x (red) and W_y (green) as a function of z as obtained from the FND. The data were fit to a defocusing function (Equations (6) and (7)). d) Distribution of the SBR calculated from FND-TGF-BSA in fixed cells (n = 322). Inset: Single molecule imaging of FND-TGF-BSA in fixed cells. e) Localization accuracy of FND-TGF-BSA under different SBR.

compared to FND in coverslips but still within excellent range. These results demonstrate that FNDs provide higher localization accuracy and resolution than those reported earlier for organic dyes and fluorescent proteins[20,22] due to its superior optical properties. The above measured localization accuracy only accounts for the focal plane. To estimate the localization accuracy in defocus plane in cells, we specifically imaged FND-TGF-BSA in the boundary of sensitive z range in fixed cells which is 360 nm away from the focal plane. It was found that the average localization accuracy in the defocus image plane (360 nm away) was 10 nm in xy and 19 nm in z (Figure S3c, Supporting Information). Compared to the localization accuracy in the focal plane, the lateral (xy) and axial (z) values decrease by 1.3-fold and 1.2-fold, respectively. The brightness of FND-TGF-BSA was further quantified (Equation (13)) as 46 100 ± 8059 photons s^{-1} (n = 10, mean ± SD). The FND provides much higher brightness compared to bright organic dye reported previously[23] for single molecule imaging. Furthermore, the average signal to noise (SNR) of FND-TGF-BSA can be easily calculated as ≈48 in both fixed cells and in vitro (Equation (15)) based on the photons emitted per frame.

2.2. Single Molecule Imaging of FND-TGF Trafficking in Live Cells

Biocompatibility is a major concern for live cell imaging applications. To evaluate the cytotoxicity of FNDs, cells treated with different doses of FNDs were examined by methyl thiazolyl tetrazolium (MTT). Treatment with 100 µg FNDs was nontoxic and biocompatible (Figure S4a, Supporting Information), consistent with previous reports.[24] In order to evaluate the preparation and functionality of FND-TGF-BSA, we decided to measure the phosphorylation state of Smad in the cells treated with different conditions (FND-TGF-BSA, ligand only and bare FNDs). Smad phosphorylation state determines nuclear transport, transcriptional activity and is thus the most critical event in TGF-β signaling.[25] We found that both FND-TGF-BSA and the ligand only (TGF-β1) can active the TGF-β receptor and subsequently phosphorylate Smad2 while the bare FND cannot (Figure S4b, Supporting Information). This result demonstrates that the as-prepared FND-TGF-BSA has good biological activity and function. We then incubated HCC827 cells with FND-TGF-BSA and unconjugated FND-PEG. Autofluorescence, which is mostly emitted from intrinsically fluorescent molecules, including pyridinic, nicotinamide adenine dinucleotide phosphate (NADPH), collagen, and flavoproteins,[26] typically contaminates the fluorescence signal at 400–600 nm. We observed a strong fluorescence signal with a bandpass emission filter in the far-red range (675/67 nm) in which detection of autofluorescence is minimized. The unique properties of FNDs make it suitable for single molecule imaging in live cells. Individual bright spots were found on the cells treated with FND-TGF-BSA whereas the cells treated with the same concentration of unconjugated FND-PEG do not show fluorescence signals. These results suggest that the bioconjugated FND-TGF show specific labeling of target proteins. Additional control experiment was performed to further evaluate the specificity of FND-TGF-BSA binding to TGF-β. In the control experiment, TGF-β in HCC827 cells was first fully blocked by two specific antibodies (anti-TGF β Receptor I and anti-TGF β Receptor II, Sigma) at 37 °C for an hour at concentration of 5 µg mL^{-1}. Then the cells were incubated with FND-TGF-BSA for 15 min before imaging. FND-TGF-BSA showed negligible signal in the antibody pretreated HCC827 cells (Figure S5a, Supporting Information) demonstrating the FND-TGF-BSA has specific interactions with TGF-β receptor.

In vivo stability of targeting nanoparticle is important for the imaging and tracking experiments. Covalent binding to nanoparticle is generally stable enough to suffer from internalization or endocytosis of cell.[27] In this work, BSA was applied to coat the surface of FNDs. BSA was reported as excellent stabilizing agent[28] and protease inhibitors to protect from proteolytic degradation[29] which suggest that as-prepared FND-TGF-BSA would be stable for in vivo tracking. In addition, TGF-β receptors are reported to be eventually transported to organelles including endosomes.[30–32] In order to evaluate the stability of FND-TGF-BSA in cells, we incubated FND-TGF-BSA in endosomal-representative buffer reported previously[33] together with 10×10^{-6} M SMI to mimic intracellular condition for one hour. After that, the washed FND-TGF-BSA was again incubated with HCC827 and put into microscopy for imaging. Confocal image showed that the treated FND-TGF-BSA is able to bind to HCC827 cells efficiently demonstrating FND-TGF-BSA is likely stable in live cells even under SMI treatment (Figure S5b, Supporting Information).

We performed time-lapse imaging of live cells after FND-TGF-BSA (10×10^{-9} M) interaction with cells. We observed punctate spots immediately after incubation (5 min, **Figure 3**a). A large amount of FND-TGF was found in the cytoplasm (Figure 3a) after 30 min, which suggests TGF internalization is very fast and is consistent with previous biochemical measurements.[32,34] To better confirm the internalization of FNDs, we used confocal microscopy to measure the fluorescence changes at the plasma membrane and cytoplasm at different time points. The cells were treated with FND-TGF-BSA at 4 °C to prevent internalization and then immediately moved to 37 °C for imaging. We found that the FND-TGF-BSA follows a fast internalization speed within the first 30 min and a slow internalization speed after 30 min. The confocal images clearly showed that FND-TGF-BSA binds to TGF-beta receptor on the cell surface in the beginning (0 min) and then distributed into cytoplasm at later time points (30 and 60 min) (Figure S6b, Supporting Information).

We next performed 3D single molecule tracking with FND-TGF in HCC827 cells (Movie 1, Supporting Information). The use of FND-TGF allowed for the observation of TGF-β and revealed its highly heterogeneous behavior. The diffusion coefficient (D) was obtained by linear fitting the mean square displacement (MSD) for the first six time lags with $6Dt^{\alpha}$ (Equation (8)), where t is the time and α is the anomaly parameter (Equation (8)). For a diffusion coefficient less than 0.01 µm^2 s^{-1} as given by the measurement of histone H2B stable binding population in live cells,[35] the tracks are treated as immobile molecules.

We observed different trajectories of FND-TGF (Figure 3b, left). The representative immobile trajectories show a diffusion coefficient of 0.01 µm^2 s^{-1}. The anomalous trajectory has a

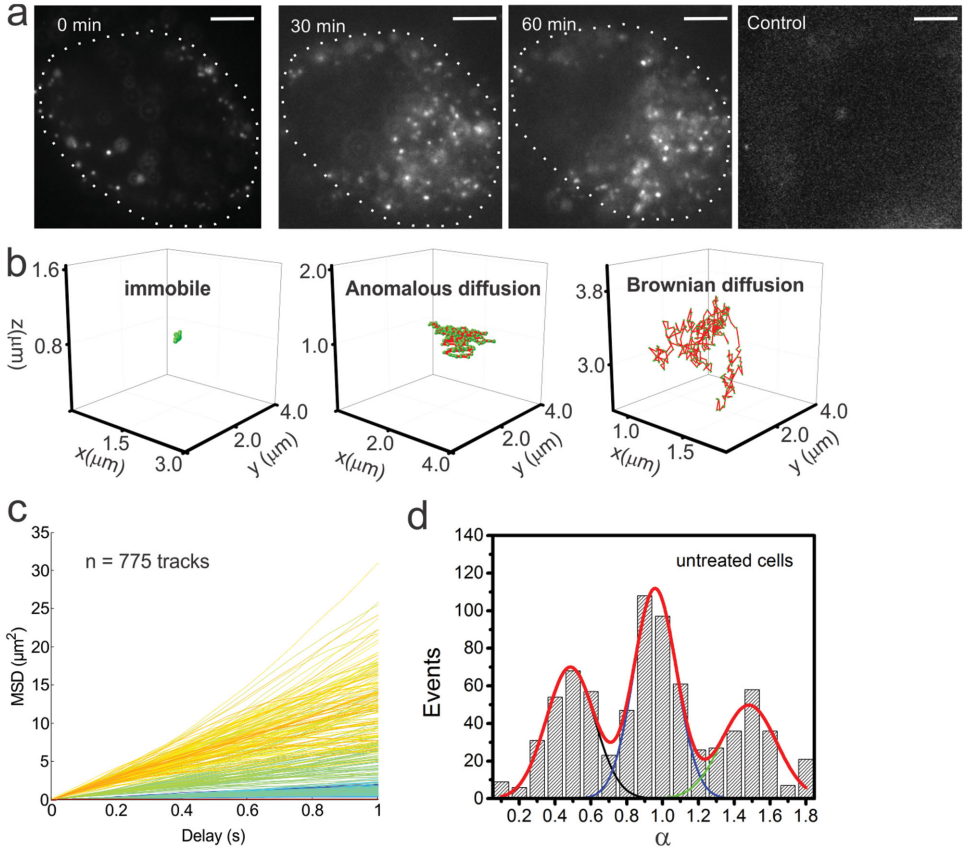

Figure 3. Single molecule imaging of FND-TGF in live cells. a) 2D image of FND-TGF in HCC827 cells at different time points (0, 30, and 60 min). Right: Control sample. HCC827 cells treated with unconjugated FND. White dotted circle represents the cell boundary. Scale bar: 3 μm. b) Representative different trajectories of FND-TGF in live cells. Left: Immobile ($D = 0.01$ μm^2 s^{-1}). Middle: Anomalous ($D = 0.2$ μm^2 s^{-1}, $\alpha = 0.6$). Right: Brownian ($D = 3$ μm^2 s^{-1}, $\alpha = 0.9$). Data were acquired at 20 Hz for 5 s. c) Individual MSD as a function of time for FND-TGF in live cells (15 cells, 775 tracks). d) Distribution of anomaly parameter (α) for FND-TGF-BSA in untreated cells. The mean value and fraction of anomaly for different population (0.48 of 32%, 0.96 of 43%, and 1.5 of 25%) were derived through fitting the distribution with three-peak Gaussian functions.

diffusion coefficient of 0.2 μm^2 s^{-1} with α at 0.6 (Figure 3b, middle) and the Brownian diffusion has a diffusion coefficient of 3 μm^2 s^{-1} with α at 0.9 (Figure 3b, right). We further plotted the MSD for all the trajectories obtained from the live cell imaging (15 cells, $n = 775$ tracks). The FNDs show a wide range of diffusion coefficients, suggesting heterogeneous behaviors (Figure 3c). To quantify the different behaviors, the distribution of diffusion coefficients was plotted and fitted with a three-peak Gaussian function (Figure S8a, Supporting Information), revealing three populations: an immobile population with D at 0.008 μm^2 s^{-1} (27.4%), an intermediate population with D at 0.24 μm^2 s^{-1} (47.7%), and a fast population with D at 2.5 μm^2 s^{-1} (24.8%).

The immobile population is likely due to the formation of active signaling complexes that contain large protein components in the plasma membrane. Similar diffusion coefficients have been reported for surface receptors in the plasma membrane.[36] The intermediate population is likely associated with anomalous diffusion on the plasma membrane and in the cytoplasm. The anomalous diffusion is thought to be due to large molecular crowding, including high densities of proteins, lipids, and organelles.[37] It was well documented that TGF-β receptors are endocytosed via clathrin-coated or lipid rafts/caveolae vesicles. After internalization, the TGF-β distributed into multiple intracellular membrane-bounded compartments. Part of the internalized vesicles are thought to be eventually transported to organelles including endosomes for signal activation or termination.[30–32] Likely, the FND-TGF-receptor complex laterally diffuses on the cell membrane and the complex went into the endosome compartment after endocytosis.[38] The fast population possibly reflects free, inactivated, or transported TGF-β that is not associated with other binding partners.

We also observed that the trajectories exhibited movement suggestive of linear and directed displacement. These results suggest the FND-TGF is actively transported through clathrin-coated vesicle-mediated endocytosis. To quantify the dynamics of active transport, we calculated the instantaneous diffusion coefficients (D_{in}) with a sliding window size of ten frames for each track. Tracks showing a transition from immobile to mobile status of D_{in} were identified as directed displacement. The movement distance and duration of active transport were then derived from the identified tracks. We found the average active transport distance is 0.7 ± 0.16 μm and the mean duration is 0.67 ± 0.15 s. Therefore, the active transport speed of FND-TGF is 1 μm s^{-1} (Figure S7, Supporting Information). Meanwhile, the velocity can be calculated through fitting the

mean active transport MSD to directed motion with diffusion equation (Equation (14))[39] and the velocity is extracted as 1.2 μm s^{-1} (Figure S7, Supporting Information). This result is similar to instantaneous diffusion coefficient calculation validating the values.

2.3. Single Molecule Imaging of FND-TGF with Small Molecule Kinase Inhibitors

Therapeutics for TGF-β-associated cancers are being developed that target TGF-β signaling,[4] including the use of neutralizing antibodies that target ligands and receptors,[40] SMI against TGF-β kinase,[41,42] and antisense oligonucleotides.[43] Although SMIs are advantageous because they are inexpensive to produce and are easy to administer orally, the exact mechanism of these drugs is not known. Here, we studied how LY2157299,[41] an SMI targeting the TGF-β serine/threonine kinase that has antitumor effects in patients with glioblastoma and hepatocellular carcinoma, changes the dynamics of TGF-β activities in live cells. Single molecule tracking of FND-TGF in cells treated with SMI were studied (Movie 2, Supporting Information).

We found the trajectories of FND-TGF to be mostly punctate spots and spatially restricted in cells without SMI (**Figure 4**a, left) compared to the cells treated with SMI (Figure 4a, right). The MSD plot in cells treated with SMI also shows a variety of different diffusion behaviors (Figure 4b), which is similar to untreated cells (Figure 3c). However, the distribution of the diffusion coefficients for cells treated with SMI shows a dramatic change in the fraction of the subpopulation (Figure S8b, Supporting Information). The histogram was fitted with a three-Gaussian function with an immobile population (0.01 $\mu m^2 s^{-1}$), an intermediate population (0.32 $\mu m^2 s^{-1}$), and a fast diffusion population (2.7 $\mu m^2 s^{-1}$). The immobile fraction, which is mostly likely located on the surface of the cells, significantly decreased from 27.4% in untreated cells to 5.3% after SMI treatment ($p < 0.01$), possibly due to LY2157299 inhibiting the formation of signaling complexes. In contrast, the fraction of intermediate and fast populations increased from 47.7% to 58.8% ($p < 0.05$) and from 24.8% to 35.9% ($p < 0.05$), respectively. Furthermore, the mean diffusion coefficients for all the tracks (including fast, intermediate and slow diffusion population) significantly increased from 0.38 $\mu m^2 s^{-1}$ in untreated cells to 1.0 $\mu m^2 s^{-1}$ ($p < 0.05$) after SMI treatment (Figure 4d). These results suggest that the blockage of the TGF-β signaling pathway could possibly release the immobilized TGF-β population, allowing more TGF-β to freely diffuse and undergo active transport in the cytoplasm. To further confirm the results from diffusion coefficient analysis, the anomaly (α) parameter obtained through fitting the MSD (Equation (8)) in untreated cells and cells treated with SMI are calculated. The distribution of alpha for both untreated and cells treated with SMI was plotted and fitted with a three-peak Gaussian function, revealing three populations: subdiffusion with α at 0.48 for untreated and 0.41 for SMI treated cells,

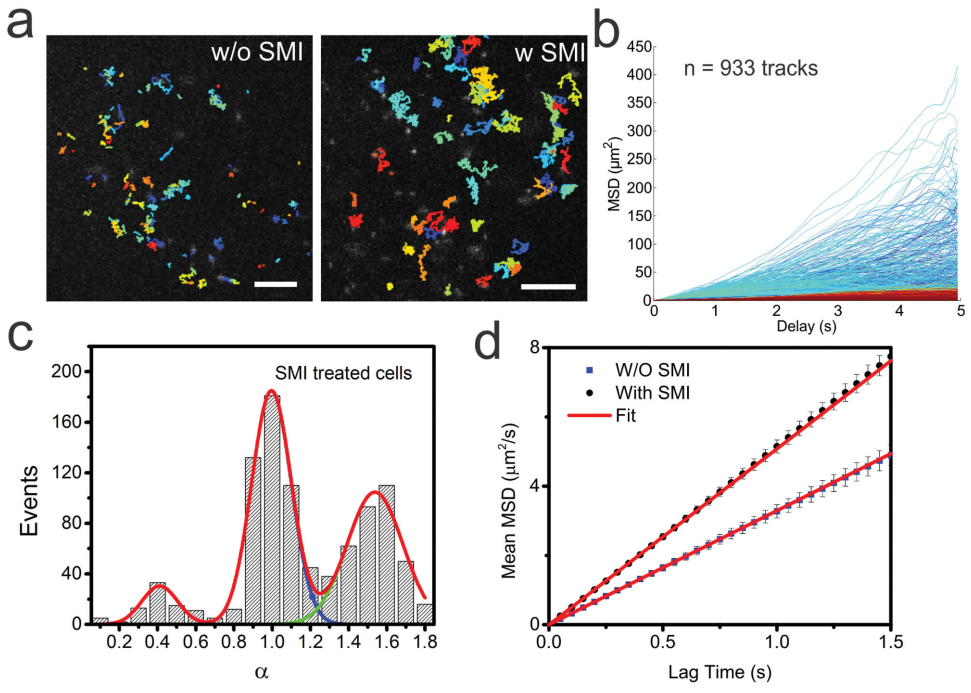

Figure 4. Single molecule imaging of FND with small molecule inhibitor (SMI) treatment. a) FND-TGF single molecule trajectories overlaid with wide-field fluorescence images in cells without SMI (left) and with SMI (right). Color corresponds to the track numbers. Scale bar: 3 μm. b) Individual MSD as a function of time for FND-TGF when treated with SMI ($n = 933$ tracks). c). Distribution of anomaly parameter (α) for FND-TGF-BSA in SMI treated cells. The mean value and fraction of anomaly for different population (0.41 of 8%, 1 of 51%, and 1.54 of 41%) were derived through fitting the distribution with three-peak Gaussian functions. d) Average MSD of FND-TGF in cells treated with SMI (black) and without SMI (blue). Red solid line is the linear fitting of the MSD. Data are expressed as mean ± standard error.

Brownian diffusion with α at 0.96 for untreated and 1 for SMI treated cells and superdiffusion with α at 1.5 for untreated and 1.54 for SMI treated cells (Figures 3d and 4c). The different anomaly values likely corresponding to slow ($\alpha < 0.9$), intermediate ($0.9 < \alpha < 1.1$), and fast ($\alpha > 1.1$) diffusion behaviors. While the anomaly values for different population are similar in the untreated cells compared to SMI treated cells, the fraction of subdiffusion population decreased from 32% to 8%. The fraction of Brownian diffusion and superdiffusion population increased from 43% to 51% and from 25% to 41%, respectively. This result confirms our diffusion coefficient distribution analysis.

To confirm and quantify the different diffusive states and the changes in states after treatment, we used a variational Bayesian treatment of a hidden Markov model (HMM)[44] to analyze the single molecule tracking data of FNDs in untreated and SMI-treated cells (Equations (9) and (10)). The variational HMM has the advantage that no presumptions of the number of states are required. We found that the best fit was achieved by a three state model, with diffusion constants of 0.02, 0.32, and 2.4 $\mu m^2\ s^{-1}$ for untreated cells (**Figure 5**a) and 0.04, 0.35, and 2.3 $\mu m^2\ s^{-1}$ for cells treated with SMI (Figure 5b). The immobile fraction decreased from 31.2% in untreated cells to 7.1% ($p < 0.05$) after SMI treatment. The fraction of intermediate and fast population increased from 50.6% to 58.4% ($p < 0.05$) and from 18.2% to 34.2% ($p < 0.05$), respectively. This observed heterogeneous diffusion behavior is consistent with the aforementioned analysis. More importantly, the transition rate per second between different statuses was derived from variational HMM (Figure 5). We found that the transition rate of changing from immobile to intermediate status increased significantly (from 0.8 to 1.6 s^{-1}, $p < 0.05$) and the transition rate of changing from fast to intermediate population (from 7.2 to 4.4 s^{-1} $p < 0.05$) decreased significantly after SMI treatment, demonstrating that the kinetic reaction favors intermediate and fast diffusion populations. This analysis confirms that SMI can release the immobilized TGF-β population for faster diffusion.

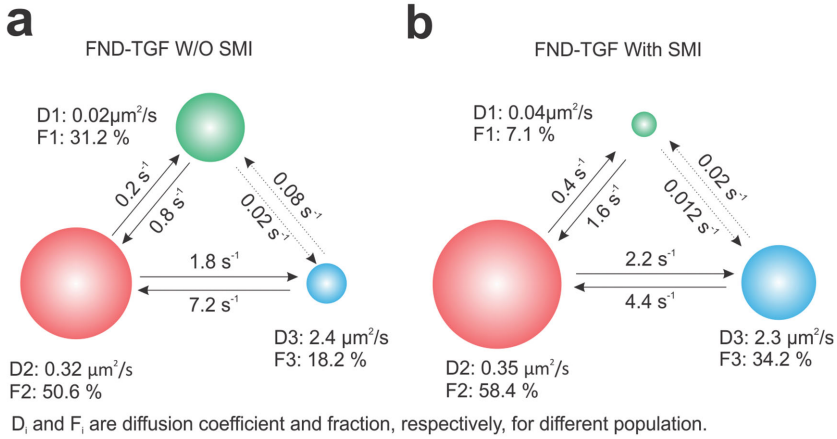

Figure 5. Kinetic analysis of FND-TGF dynamics of different states by Hidden Markov models. Green: immobile state; red: intermediate state; and blue: fast diffusion state. a) Untreated cells b) Cells treated with SMI. Trajectories longer than four steps are applied for analysis. The transition rate (per second), diffusion coefficient (D), and fraction (F) are derived from the analysis. The size of the ball corresponds to the fraction of different population.

3. Conclusion

In this work, we demonstrate that FNDs can be used as a specific endogenous protein tag for long-term imaging due to its superior optical properties, biocompatibility, and ease of functionalization. Moreover, it provides ultrahigh localization accuracy in 3D for nanoscopy applications. Combining FNDs with 3D single molecule imaging techniques, we monitored the direct trafficking process of discrete TGF-β signaling. The TGF-β showed a highly heterogeneous behavior in cells revealing three different states: immobile, intermediate, and fast diffusion. After SMI treatment, the immobile population significantly decreased while the intermediate and fast population increased. Furthermore, variational Bayesian HMM analysis showed that therapeutic SMI could change the transition rates dramatically between the three states and push the kinetic reaction toward intermediate and fast diffusion states. Our results reveal that immobilized TGF-β is critical for the active signaling pathway and SMI treatment could increase the diffusion coefficient of TGF-β by releasing it from large binding complexes. Our work introduces a novel application of FNDs as specific endogenous protein tags in live cells to study transmembrane signaling function and dynamics. This method can be used to investigate how a drug influences the dynamic behaviors of the target protein in live cells. This provides an unprecedented opportunity to understand the mechanisms of the TGF-β pathway and aid our development of better therapeutic strategies to treat TGF-β-associated cancers.

4. Experimental Section

Cell Culture and Buffers: The human lung adenocarcinoma cell line HCC827 was obtained from American-type culture collection (ATCC). HCC827 cells were grown in Roswell Park Memorial Institute (RPMI) 1640 (Hyclone) media supplemented with 10% fetal bovine serum. Cells were maintained in an incubator at 37 °C with 5% CO_2. For live cell fluorescence microscopy studies, cells were seeded onto a sterilized No. 1.5 coverslip (VWR International, Batavia, IL) and placed inside a six-well plate. The coverslips are cleaned with Piranha solution[45] (70% sulfuric acid (99% w/v) and 30% hydrogen peroxide (35% w/v). LY2157299 was purchased from Cayman Chemical. Endosomal-representative buffer was prepared based on previously report[33] (44×10^{-3} M citric acid, 156×10^{-3} M dibasic sodium phosphate, and 17×10^{-3} M L-cysteine, pH = 6). Anti-TGF β Receptor I (SAB2700824) and anti-TGF β Receptor II (SAB4502960) were purchased from Sigma.

Fluorescent Nanodiamond Preparation: Fluorescent nanodiamonds were synthesized according to a previously described method.[16] Briefly, 40 nm type Ib nanodiamonds (Guangzhou Fanxing Trading Co., China) were treated using a electronic irradiation beam in Gy Irradiation Technology Co., Ltd. (Shenzhen, China) to create vacancies in the diamond crystal. FNDs were formed with thermal annealing in a vacuum at 800 °C for 2 h. FNDs were then washed in distilled deionized water and stored at room temperature. FNDs were surface functionalized with carboxyl groups in concentrated H_2SO_4-HNO_3 (3:1, v/v) at 100 °C for 3 h.

Covalent Conjugation of FNDs with Streptavidin: FNDs were conjugated with streptavidin according to a previously described method.[17] Briefly, 1-ethyl-3-(3-dimethylaminopropyl)carbodiimide (EDAC) and Sulfo-NHS (Thermo Scientific, USA) were added to activate the carboxyl groups. Then, the FNDs were PEGylated by adding *O*-(2-aminoethyl)-*O′*-(2-carboxyethyl)polyethylene glycol hydrochloride (Sigma-Aldrich) for 6 h. After washing with deionized water, the PEG-FND was activated by EDAC and Sulfo-NHS to react with streptavidin (Thermo Scientific) for 4 h. The SA-PEG-FND particles were coated with BSA for 2 h.

Conjugation of FNDs with TGF: TGF (TGF-beta1, R&D Systems, USA) was biotinylated through carboxyl group substitution using sulfo-NHS-biotin (Thermo Scientific, USA) at stoichiometric ratios that resulted in two or less biotins per TGF. The biotinylated TGF was purified using a protein concentrator (9K MWCO, Thermo Scientific, USA).

FND-TGF complexes were formed by gentle vortexing and incubating biotinylated TGF with SA-PEG-FND at a 1:1 molar ratio (4 °C, 1 h). The FND-TGF was purified by centrifugation at 6000 rpm for 10 min. After conjugation, a small amount of FND-TGF solution was dispersed and imaged on glass coverslip for characterization.

Cell Proliferation Assay: HCC827 cells cultured in medium free of phenol red were seeded in a 96-well plate at a density of 10^4 cells per well in a 100 µL volume. Cells were maintained at 37 °C for 24 h after treatment with FNDs of different concentrations. Cell viability was then determined based on reduction activity of MTT assay (Vybrant MTT cell proliferation Kit, Life Technologies). The FND-treated cells were incubated with the MTT reagent for 3 h at 37 °C. sodium dodecyl sulfateHCL (SDS-HCL) solution (100 µL) was added to each well with thorough mixing, followed by incubation for 1 h. The absorbance at 570 nm was read. The results are expressed as percentages.

Western Blot Analysis of Smad2 Phosphorylation: HCC827 cells were first treated with FND-TGF, TGF-β1, or FND for 30 min, respectively. After that, the cells were washed with cold tris-buffered saline (TBS) buffer, collected by manual scraping using a rubber policeman and pelleted by centrifugation. The cell pellet was suspended in gentle lysis buffer (10×10^{-3} M Tris-HCl at pH 7.5, 10×10^{-3} M NaCl, 10×10^{-3} M ethylenediaminetetraacetic acid (EDTA), 1% TritonX-100, 1 × phosphatase inhibitor cocktail (Roche), 1 × protease inhibitor cocktail (Roche), 1×10^{-3} M dithiothreitol (DTT) and 10 mg mL^{-1} of RNase A) and incubated on ice for 15 min. The insoluble materials were removed by centrifugation at 13 400 g in a microcentrifuge at 4 °C for 15 min. 30 µg total protein was resolved by sodium dodecyl sulfate polyacrylamide gel electrophoresis (SDS-PAGE), followed by western blot analysis using Phospho-Smad2 (Ser465/467) Antibody (#3101, Cell Signaling Technology) or Smad2 antibody (#3122, Cell Signaling Technology).

3D Single Molecule Microscopy: The 3D single-molecule experiments were performed on a home-built Nikon Ti-E microscope coupled with a 100× oil-immersion objective lens (Nikon, NA = 1.49). The microscope was equipped with a multiband dichroic (405/488/561/633 BrightLine quad-band bandpass filter, Semrock, USA), a piezo *z*-stage (Nano-Z Series, Madcity Lab Inc., USA) and live cell incubator (Okolab). The laser (561 nm; OBIS, Coherent, USA) with reflected from the multiband dichroic mirror was focused into the back focal plane of the objective to generate wide-field illumination (1 KW cm^{-2}). The emission was collected by the same objective passing through a single-band bandpass filter (675/67 nm, Semrock, USA). A cylindrical lens (focal length = 1 m) was placed in front of the EMCCD (iXon X3 DU-897, Andor Technologies, USA) to introduce spherical aberration to distort the symmetric point spread function (PSF) of the dipole emission into an elliptical point spread function (PSF) whose aspect ratio depended on the precise *z* position as described by Huang et al.[20] The microscope, lasers, emission filters, and the camera were controlled through μ-manager. All live cell imaging experiments were performed at 37 °C with 5% CO_2. The acquisition time for all the 3D single molecule tracking is 50 ms (20 Hz). All the single molecule tracking experiments in untreated and cells treated with SMI are performed in the well-controlled same condition. The cells were incubated for 30 min at 37 °C with 10×10^{-9} M FND-TGF-BSA in phenol red free Opti-MEM I medium before imaging was conducted. Typically, tracking were collected with a short period time (2500 frames) per cell for both conditions.

In Vitro Single Molecule Imaging of FNDs by TIRF: To characterize optical properties, individual FNDs were imaged on clean coverslips using the same home-built microscope described above with total internal reflection fluorescence (TIRF) illumination. In TIRF, fluorescent molecules are excited by an evanescent wave generated by reflecting a laser beam off the coverglass when the laser reaches a critical angle. Because of the weak nature of this energy field and the thin *z* depth coverage, it provides a very high signal-to-noise ratio for single molecule imaging. The No. 1.5 coverslips were cleaned with Piranha solution. Subsequently, coverslips were thoroughly cleaned with Millipore water multiple times. Then, 200 µL of FNDs was deposited onto the cleaned coverslips for 10 min, following which the coverslips were washed three times before imaging. A 100× Oil-immersion TIRF objective lens (Nikon, NA = 1.49) was used to achieve objective-type total internal reflection. The incident angle of 561 nm laser was varied until it reached a critical angle for the imaging of individual FNDs on the coverslip. The emission was collected by the same objective and collected by a bandpass filter (675/67 nm, Semrock, USA).

Confocal Microscopy of FND Internalization: Confocal images were taken with a Zeiss 710 system (Zeiss, Germany). An oil-immersion 63× objective lens (NA = 1.4) was used. The samples were excited with a laser at 561 nm, and the fluorescence was detected using a GaAsP detector in the range of 640–700 nm. A pinhole size at 1 airy unit was set during confocal image acquisition with a live-cell-compatible stage at 37 °C with 5% CO_2 supply.

Fluorescence Correlation Spectroscopy for FND: FCS measurements were performed using a scanning confocal microscope (Olympus, Japan) with a Picoquant FCS upgrade system (Picoquant, Germany). A 561 nm laser (Melles Griot, USA) was used as an illumination source and delivered to the sample through an apochromatic 60×, 1.2 NA water immersion objective (Olympus, Japan). The emitted fluorescence was reflected by a dichroic mirror (ZT594rdc-UF2, Chroma) and filtered by emission filters (675/67 nm, Semrock, USA) before detection by single photon avalanche photodiodes (SPCM, PerkinElmer Inc.).

In FCS measurements, the fluorescent intensity as a function of time ($F(t)$) was recorded. The time-dependent fluorescence fluctuations $\delta F(t)$ around the average values were thus obtained. The normalized autocorrelation function was calculated based on the following equation

$$G(\tau) = \frac{\langle \delta F(t) \times \delta F(t+\tau) \rangle}{\langle F(t) \rangle^2} \tag{1}$$

where $\langle F(t) \rangle$ stands for the mean value and τ is the time delay. The autocorrelation function of FNDs was fitted into a 3D diffusion model[46]

$$G(\tau) = \frac{1}{N}\left(1+\frac{\tau}{\tau_D}\right)^{-1}\left(1+\frac{\tau}{\tau_D \times \text{kappa}^2}\right)^{-1/2} \tag{2}$$

where N and τ_D are the number of fluorescent molecules in the detection volume and diffusion time of the fluorescence molecules, respectively, and kappa is defined as the ratio of the axial beam size z and radius ω. The diffusion time is defined as

$$\tau = \frac{\omega}{4D} \tag{3}$$

where D is the diffusion coefficient. The effective confocal volume was calibrated using Alexa Fluo 546 dye (Life Technology) with a known diffusion coefficient of 341 $\mu m^2\ s^{-1}$.[47] Assuming a 3D Gaussian confocal beam, the volume was approximated by

$$V_{\text{eff}} = \pi^{3/2}\omega^2 z \tag{4}$$

The size of the FNDs can be calculated through the Stokes–Einstein equation based on the diffusion coefficient measured by FCS

$$D = \frac{kT}{6\pi\eta r} \tag{5}$$

where η is the viscosity of the medium, k is Boltzmann's constant, T is the absolute temperature, and r is the radius of the particle.

Analysis of FND Single Molecule Trajectories: The PSF were fitted using a 2D asymmetric Gaussian fit

$$G(x,y) = a + bexp\left(-\frac{(x-x_0)^2}{2w_x^2} - \frac{(y-y_0)^2}{2w_y^2}\right) \tag{6}$$

where (x_0, y_0) is the center position of the peak and w_x and w_y are the widths of the PSF. FNDs were used to calibrate the absolute z position at a step size of 10 nm using the piezo z stage. The w_x and w_y were correlated to the z-position relative to the focal plane based on the calibration data. The w_x and w_y as a function of z was fitted with a defocusing function as described in a previous report[20]

$$w_{x,y}(z) = w_0\sqrt{1+\left(\frac{z-a}{d}\right)^2 + b\left(\frac{z-a}{d}\right)^3 + c\left(\frac{z-a}{d}\right)^4} \tag{7}$$

where a is the offset of the x or y focal plane from the average focal plane and d is the focus depth.

After obtaining the 3D localization, the 3D single molecule tracking was performed based on u-Track algorithm.[48] In order to determine the optimal number of MSD points to obtain the best estimate of D, a control parameter named the reduced localization error $x = \sigma^2/D\Delta t$ is calculated.[49,50] When $x \ll 1$, a short time lags give the optimal fitting of D; When $x \gg 1$, a larger number of MSD points are needed to obtain a reliable estimate of D. In our case, this dimensionless ratio was derived $x \ll 1$. Therefore, the diffusion coefficient of the FND was calculated based on fitting the MSD of the molecules for the first six time lapses and analyzed with an MSD analyzer.[51]

The mean square displacement of molecules in 3D is described as follows

$$\langle r^2 \rangle = 6Dt^{\alpha} \tag{8}$$

where D is the diffusion coefficient of the fluorescence molecules, t is the time, and r^2 is the mean square displacement. $0.9 < \alpha < 1.1$ indicates Brownian diffusion; $\alpha > 1.1$,[52] superdiffusion (e.g., active transport); and $0.1 < \alpha < 0.9$,[53] subdiffusion (e.g., anomalous).[54–56] The diffusion coefficient histogram was then fitted with three-Gaussian peak to distinguish subpopulations.

Bayesian Treatment of HMM Analysis: HMM analysis of the single particle tracking data was carried out with a modified vbSPT program originally developed by Persson et al.[44] The expressions for the joint distribution of positions, hidden states, and parameters, can be factorized as

$$\begin{aligned} &p\left(\vec{x}_{1:T}, s_{1:T-1}, \vec{D}, A, \vec{\pi}|N\right) \\ &= p\left(\vec{x}_{1:T}|s_{1:T-1}, \vec{D}\right)p\left(s_{1:T-1}|A, \vec{\pi}\right) \\ &\quad \times p\left(\vec{D}|N\right)p(A|N)p(\vec{\pi}|N) \end{aligned} \tag{9}$$

The left side of the equation is the parameter and the first two items on the right side are distribution of positions and conditional and hidden states. In particular

$$p\left(s_{1:T-1}|A, \vec{\pi}\right) = \pi_{s1}\prod_{t=1}^{T-2} A_{s_t, s_{t+1}} \tag{10}$$

The results were computed on Matlab 2013a with a parallel computation toolbox.

Characterization of FND-TGF-BSA: The size distribution of FND-TGF-BSA in water was performed using DLS by Malvern Zetasizer 3000 E (Malvern, UK). The morphology and size of the FND-TGF were characterized using TEM (Tecnai G2 20, FEI, The Netherlands).

To quantify the number of TGF attached to the surface of the FNDs, we first estimated the concentration of FNDs by FCS. The number of molecules (N) in the confocal volume was obtained through fitting the autocorrelation function with Equation (2). For time $\tau = 0$, the amplitude of autocorrelation provides a measure of the average number of molecules in the confocal volume given by

$$G(0) = \frac{1}{N} = \frac{1}{CV_{\text{eff}}} \tag{11}$$

where C is the concentration and V_{eff} is the effective confocal volume. Therefore, the concentration of FND is given by

$$C = \frac{N}{V_{\text{eff}}} \tag{12}$$

Next, the protein concentration is determined using absorbance at 280 nm. The amount of TGF conjugated to the FND was calculated using the following formula: TGF to FND = total TGF added − TGF in the supernatant solution.

To quantify the brightness of FND-TGF-BSA, the following relationship was applied

$$\text{Photons} = \frac{\text{counts} \times \text{ADU conversion factor}}{\text{EM gain} \times \text{QE}} \tag{13}$$

The analogue-to-digital unit (ADU) conversion factor can be found from the camera performance datasheet with corresponding system readout rate and Preamp setting. The counts were calculated through fitting the FND-TGF-BSA with 2D Gaussian function.

Calculation of Velocity of Active Transport Trajectories: Instantaneous diffusion coefficients (D_{in}) were calculated by linear fitting an MSD curve with a sliding window size of ten time lags. Active transport tracks were found through identifying transitions (from immobile to mobile diffusion) from the D_{in} time trace.

The velocity of active transport trajectories was calculated based on fitting the MSD with following relationship[39]

$$\langle r^2 \rangle = 6Dt^{\alpha} + (vt)^2 \tag{14}$$

The equation reflects the dominance of the active transport component at longer time.

Statistical Analysis: Data obtained have been expressed as mean ± standard deviation unless stated otherwise. The comparison was analyzed by one-way analysis of variance (ANOVA) with the post hoc Tukey's test applied for paired comparisons. The difference between means was considered significant when the P value was <0.05.

Calculation of Localization Accuracy in Relationship to Signal to Background Ratio: It was well documented that the read noise, dark counts, and spurious noise can be virtually eliminated in deep-cooled EMCCD and thus single-molecule imaging are generally limited by shot noise.[57–59] Therefore, in the case of bright sample, the SNR was defined as the following equation due to the nature of Poisson statistics

$$\text{SNR} \approx \sqrt{N} \tag{15}$$

where N is the number of photons recorded in a frame of data.

The theoretic localization accuracy was reported by Thompson[60] as

$$\left\langle (\Delta x)^2 \right\rangle = \frac{s^2}{N} + \frac{a^2/12}{N} + \frac{4\sqrt{\pi s^3 b^2}}{aN^2} \tag{16}$$

where Δx is localization error, s is the width (sigma) of the PSF from Gaussian fitting, N is the number of photons, and b is the background noise. In the case of high photon numbers which is the case in our study, the localization precision Δx can be approximately as $S/\sqrt{N}$ in normal 2D Gaussian fitting.

The SBR was defined as dividing the signal by background. The SBR for FND-TGF-BSA population in the fixed cells was first calculated. Then the 95% confidence interval of SBR was estimated based on the 5% and 95% quantile for nonnormal distribution data.[61] The FND-TGF-BSA with different SBR was imaged continuously for 1000 frames followed by 3D localization to measure the localization accuracy.

Supporting Information

Supporting Information is available from the Wiley Online Library or from the author.

Acknowledgements

W.L. and F.Y. contributed equally to this work. This work was supported by the National Natural Science Foundation of China (Grant 81101767 to L.W.), the Specialized Research Fund for the Doctoral Program of Higher Education (Grant 20110162120018 to L.W.), and the Hunan Provincial Natural Science Foundation of China (Grant 14JJ2029 to W.L.). The authors thank Dr. Richard Battafarano (John Hopkins University, USA) for the insights and Prof. Guofu Xu (Central South University), and Prof. Shaojun Liu (Central South University) for assistance with the experiments.

Received: July 13, 2015
Revised: October 12, 2015
Published online: December 7, 2015

[1] M. B. Sporn, A. B. Roberts, L. M. Wakefield, R. K. Assoian, *Science* **1986**, *233*, 532.
[2] K. J. Gordon, G. C. Blobe, *Biochim. Biophys. Acta* **2008**, *1782*, 197.
[3] S. B. Jakowlew, *Cancer Metastasis Rev.* **2006**, *25*, 435.
[4] R. J. Akhurst, A. Hata, *Nat. Rev. Drug Discovery* **2012**, *11*, 790.
[5] Y. Shi, J. Massague, *Cell* **2003**, *113*, 685.
[6] R. Derynck, Y. E. Zhang, *Nature* **2003**, *425*, 577.
[7] M. Arjaans, T. H. Oude Munnink, H. Timmer-Bosscha, M. Reiss, A. M. Walenkamp, M. N. Lub-de-Hooge, E. G. de Vries, C. P. Schroder, *Pharmacol. Ther.* **2012**, *135*, 123.
[8] R. Schirhagl, K. Chang, M. Loretz, C. L. Degen, *Annu. Rev. Phys. Chem.* **2014**, *65*, 83.
[9] N. Mohan, C. S. Chen, H. H. Hsieh, Y. C. Wu, H. C. Chang, *Nano Lett.* **2010**, *10*, 3692.
[10] C. C. Fu, H. Y. Lee, K. Chen, T. S. Lim, H. Y. Wu, P. K. Lin, P. K. Wei, P. H. Tsao, H. C. Chang, W. Fann, *Proc. Natl. Acad. Sci. USA* **2007**, *104*, 727.
[11] J. Tisler, R. Reuter, A. Lammle, F. Jelezko, G. Balasubramanian, P. R. Hemmer, F. Reinhard, *ACS Nano* **2011**, *5*, 7893.
[12] O. Faklaris, V. Joshi, T. Irinopoulou, P. Tauc, M. Sennour, H. Girard, C. Gesset, J. C. Arnault, A. Thorel, J. P. Boudou, P. A. Curmi, F. Treussart, *ACS Nano* **2009**, *3*, 3955.
[13] L. M. Manus, D. J. Mastarone, E. A. Waters, X. Q. Zhang, E. A. Schultz-Sikma, K. W. Macrenaris, D. Ho, T. J. Meade, *Nano Lett.* **2010**, *10*, 484.
[14] G. Xi, E. Robinson, B. Mania-Farnell, E. F. Vanin, K. W. Shim, T. Takao, E. V. Allender, C. S. Mayanil, M. B. Soares, D. Ho, T. Tomita, *Nanomedicine* **2014**, *10*, 381.
[15] X. Q. Zhang, M. Chen, R. Lam, X. Xu, E. Osawa, D. Ho, *ACS Nano* **2009**, *3*, 2609.
[16] Y. R. Chang, H. Y. Lee, K. Chen, C. C. Chang, D. S. Tsai, C. C. Fu, T. S. Lim, Y. K. Tzeng, C. Y. Fang, C. C. Han, H. C. Chang, W. Fann, *Nat. Nanotechnol.* **2008**, *3*, 284.
[17] B. M. Chang, H. H. Lin, L. J. Su, W. D. Lin, R. J. Lin, Y. K. Tzeng, R. T. Lee, Y. C. Lee, A. L. Yu, H. C. Chang, *Adv. Funct. Mater.* **2013**, *23*, 5737.
[18] L. Wang, X. Li, B. Xiang, M. Zhou, X. Li, W. Xiong, M. Niu, P. Wei, Z. Wang, H. Wang, P. Chen, S. Shen, S. Peng, G. Li, *J. Biol. Chem.* **2014**, *289*, 35731.
[19] M. A. Digman, E. Gratton, *Annu. Rev. Phys. Chem.* **2011**, *62*, 645.
[20] B. Huang, W. Q. Wang, M. Bates, X. W. Zhuang, *Science* **2008**, *319*, 810.
[21] H. P. Kao, A. S. Verkman, *Biophys. J.* **1994**, *67*, 1291.
[22] M. Lakadamyali, H. Babcock, M. Bates, X. Zhuang, J. Lichtman, *PLoS One* **2012**, *7*, e30826.
[23] J. B. Grimm, B. P. English, J. Chen, J. P. Slaughter, Z. Zhang, A. Revyakin, R. Patel, J. J. Macklin, D. Normanno, R. H. Singer, T. Lionnet, L. D. Lavis, *Nat. Methods* **2015**, *12*, 244.
[24] S. J. Yu, M. W. Kang, H. C. Chang, K. M. Chen, Y. C. Yu, *J. Am. Chem. Soc.* **2005**, *127*, 17604.
[25] K. H. Wrighton, X. Lin, X. H. Feng, *Cell Res.* **2009**, *19*, 8.
[26] M. Monici, *Biotechnol. Annu. Rev.* **2005**, *11*, 227.
[27] C. Harding, J. Heuser, P. Stahl, *J. Cell Biol.* **1983**, *97*, 329.
[28] P. Khullar, V. Singh, A. Mahal, P. N. Dave, S. Thakur, G. Kaur, J. Singh, S. S. Kamboj, M. S. Bakshi, *J. Phys. Chem. C* **2012**, *116*, 8834.
[29] L. Nagy, B. R. Johnson, P. Hauschka, S. Szabo, *Am. J. Physiol.* **1997**, *272*, G1151.
[30] Y. G. Chen, *Cell Res.* **2009**, *19*, 58.
[31] G. M. Di Guglielmo, C. Le Roy, A. F. Goodfellow, J. L. Wrana, *Nat. Cell Biol.* **2003**, *5*, 410.
[32] J. C. Zwaagstra, M. El-Alfy, M. D. O'Connor-McCourt, *J. Biol. Chem.* **2001**, *276*, 27237.
[33] S. Jordans, S. Jenko-Kokalj, N. M. Kuhl, S. Tedelind, W. Sendt, D. Bromme, D. Turk, K. Brix, *BMC Biochem.* **2009**, *10*, 23.
[34] H. Mitchell, A. Choudhury, R. E. Pagano, E. B. Leof, *Mol. Biol. Cell* **2004**,. *15*, 4166.
[35] D. Mazza, A. Abernathy, N. Golob, T. Morisaki, J. G. McNally, *Nucleic Acids Res.* **2012**, *40*, e119.
[36] F. Daumas, N. Destainville, C. Millot, A. Lopez, D. Dean, L. Salome, *Biophys. J.* **2003**, *84*, 356.
[37] J. A. Dix, A. S. Verkman, *Annu. Rev. Biophys.* **2008**, *37*, 247.
[38] K. M. Fichter, M. Flajolet, P. Greengard, T. Q. Vu, *Proc. Natl. Acad. Sci. USA* **2010**, *107*, 18658.
[39] M. J. Saxton, K. Jacobson, *Annu. Rev. Biophys. Biomol. Struct.* **1997**, *26*, 373.
[40] F. Bouquet, A. Pal, K. A. Pilones, S. Demaria, B. Hann, R. J. Akhurst, J. S. Babb, S. M. Lonning, J. K. DeWyngaert, S. C. Formenti, M. H. Barcellos-Hoff, *Clin. Cancer Res.* **2011**, *17*, 6754.
[41] J. Rodon, M. A. Carducci, J. M. Sepulveda-Sanchez, A. Azaro, E. Calvo, J. Seoane, I. Brana, E. Sicart, I. Gueorguieva, A. L. Cleverly, N. S. Pillay, D. Desaiah, S. T. Estrem, L. Paz-Ares, M. Holdhoff, J. Blakeley, M. M. Lahn, J. Baselga, *Clin. Cancer Res.* **2015**, *21*, 553.
[42] G. Giannelli, E. Villa, M. Lahn, *Cancer Res.* **2014**, *74*, 1890.
[43] U. Bogdahn, P. Hau, G. Stockhammer, N. K. Venkataramana, A. K. Mahapatra, A. Suri, A. Balasubramaniam, S. Nair, V. Oliushine, V. Parfenov, I. Poverennova, M. Zaaroor, P. Jachimczak, S. Ludwig, S. Schmaus, H. Heinrichs, K.-H. Schlingensiepen, *Neuro Oncol.* **2011**, *13*, 132.
[44] F. Persson, M. Linden, C. Unoson, J. Elf, *Nat. Methods* **2013**, *10*, 265.
[45] S. D. Chandradoss, A. C. Haagsma, Y. K. Lee, J. H. Hwang, J. M. Nam, C. Joo, *J. Visualized Exp.* **2014**, *86*, e50549.
[46] P. Schwille, F. J. Meyer-Almes, R. Rigler, *Biophys. J.* **1997**, *72*, 1878.
[47] Z. Petrasek, P. Schwille, *Biophys. J.* **2008**, *94*, 1437.
[48] K. Jaqaman, D. Loerke, M. Mettlen, H. Kuwata, S. Grinstein, S. L. Schmid, G. Danuser, *Nat. Methods* **2008**, *5*, 695.
[49] E. Kepten, A. Weron, G. Sikora, K. Burnecki, Y. Garini, *PLoS One* **2015**, *10*, e0117722.
[50] X. Michalet, *Phys. Rev. E: Stat., Nonlinear, Soft Matter Phys.* **2010**, *82*, 041914.

[51] N. Tarantino, J. Y. Tinevez, E. F. Crowell, B. Boisson, R. Henriques, M. Mhlanga, F. Agou, A. Israël, E. Laplantine, *J. Cell Biol.* **2014**, *204*, 231.
[52] I. M. Kulic, A. E. Brown, H. Kim, C. Kural, B. Blehm, P. R. Selvin, P. C. Nelson, V. I. Gelfand, *Proc. Natl. Acad. Sci. USA* **2008**, *105*, 10011.
[53] T. J. Feder, I. Brust-Mascher, J. P. Slattery, B. Baird, W. W. Webb, *Biophys. J.* **1996**, *70*, 2767.
[54] M. J. Saxton, *Biophys. J.* **1994**, *66*, 394.
[55] M. Weiss, *Int. Rev. Cell Mol. Biol.* **2014**, *307*, 383.
[56] H. Qian, M. P. Sheetz, E. L. Elson, *Biophys. J.* **1991**, *60*, 910.
[57] M. L. Martin-Fernandez, D. T. Clarke, *Int. J. Mol. Sci.* **2012**, *13*, 14742.
[58] W. E. Moerner, D. P. Fromm, *Rev. Sci. Instrum.* **2003**, *74*, 3597.
[59] H. Deschout, F. Cella Zanacchi, M. Mlodzianoski, A. Diaspro, J. Bewersdorf, S. T. Hess, K. Braeckmans, *Nat. Methods* **2014**, *11*, 253.
[60] R. E. Thompson, D. R. Larson, W. W. Webb, *Biophys. J.* **2002**, *82*, 2775.
[61] R. McGill, J. W. Tukey, W. A. Larsen, *Am. Stat.* **1978**, *32*, 12.